RF-MEMS Switches Designed for High-Performance Uniplanar Microwave and mm-Wave Circuits

Lluis Pradell, David Girbau, Miquel Ribó,
Jasmina Casals-Terré, Antonio Lázaro,
Adrián Contreras, Marco Antonio Llamas,
Julio Heredia, Flavio Giacomozzi and
Benno Margesin

Additional information is available at the end of the chapter

Abstract

Radio frequency microelectromechanical system (RF-MEMS) switches have demonstrated superior electrical performance (lower loss and higher isolation) compared to semiconductor-based devices to implement reconfigurable microwave and millimeter (mm)-wave circuits. In this chapter, electrostatically actuated RF-MEMS switch configurations that can be easily integrated in uniplanar circuits are presented. The design procedure and fabrication process of RF-MEMS switch topologies able to control the propagating modes of multimodal uniplanar structures (those based on a combination of coplanar waveguide (CPW), coplanar stripline (CPS), and slotline) will be described in detail. Generalized electrical (multimodal) and mechanical models will be presented and applied to the switch design and simulation. The switch-simulated results are compared to measurements, confirming the expected performances. Using an integrated RF-MEMS surface micromachining process, high-performance multimodal reconfigurable circuits, such as phase switches and filters, are developed with the proposed switch configurations. The design and optimization of these circuits are discussed and the simulated results compared to measurements.

Keywords: RF-MEMS switches, MEMS fabrication technology, reconfigurable microwave circuits, uniplanar multimodal circuits, circuit simulation, electromechanical simulation, filters, phase switches

1. Introduction

Radio frequency microelectromechanical system (RF-MEMS) switches are aimed to perform the control function in tunable and reconfigurable RF/microwave and millimeter-wave (mm-wave) systems. Electrostatic actuation is often preferred to other actuation mechanisms like electrothermal [1, 2] and phase-change/phase-transition materials [3], due to its negligible current consumption, no requirement for external heating sources and integration capability with well-established technologies such as high-resistivity silicon [4–7], fused-quartz and glass substrates [8–11], or CMOS [12–15] and SiGe BiCMOS [16, 17] processes. The latter can provide totally integrated, efficient systems containing sensors, control electronics, and MEMS-reconfigurable RF communication circuits [18].

The mechanical and electrical design of the RF-MEMS switches has been comprehensively studied in the literature [19], and it highly depends on the circuit or transmission media in which it is to be integrated and the technology platform [20]. A number of solutions can be found, including integration in microstrip transmission lines [21], coplanar waveguides (CPWs) [4], coplanar striplines (CPSs) and slotlines [11], planar structures embedded in rectangular waveguides [22], and micromachined waveguides for sub-mm-wave frequencies [23]. Depending on the specific designs and dimensions, they can operate in the microwave and the mm-wave bands, at frequencies as high as 240 GHz as reported in [24] using BEOL in BiCMOS technology.

Series and parallel RF-MEMS switch topologies can be implemented, with either ohmic-contact [22] or capacitive-contact [4, 25]. While ohmic switches can operate in a very wide frequency band from DC to mm-waves featuring excellent OFF-state isolation and very low ON-state insertion loss, capacitive switches are frequency selective (being the center frequency defined by a series LC-resonant circuit) but their operation can be extended well beyond mm-wave frequencies by properly choosing the ON-state capacitance and the series inductance which depends on the membrane dimensions [24].

Mechanical topologies for RF-MEMS switches include bridge-type clamped-clamped or beam-suspension membranes and cantilever-type switches. Important switch parameters, such as the actuation voltage or the fabrication residual stress, are dependent on the particular selected topology [26–28]. Using three-dimensional (3D) mechanical simulation, the material physical properties are taken into account to a priori assess the behavior of the switch geometry (including the suspension type) in terms of initial membrane deformation, pull-in voltage, spring constant, mechanical resonant frequency, and transition times from OFF to ON states (and vice versa) [29]. Mechanical transients may produce bouncing phenomena [30–34] which degrade the RF behavior of the switch and can be studied more efficiently with energy models [35].

RF-MEMS switches featuring the above mechanical topologies are compatible with and can be conveniently integrated in uniplanar structures (CPW, CPS, and slotline) to perform a control function. In case of multimodal transmission lines like CPW, they can be used to selectively control the two CPW fundamental propagation modes (even and odd) [36]. To accurately analyze the interaction between modes in complex uniplanar structures (transitions, discontinuities), multimodal circuit models are derived from the application of the general multimodal theory [37–40]. Moreover, suitable equivalent circuits for both (ON/OFF) states

of the switch can be obtained and integrated in the multimodal models. In this way, efficient and compact reconfigurable circuits for communication systems at microwave and mm-wave frequencies can be designed [6, 9–11].

In this chapter, a detailed study of RF-MEMS switches to be used in multimodal uniplanar circuits is presented. The switch electromechanical design considerations are explained in detail, and a number of switch configurations proposed, simulated mechanically, and fabricated using the FBK flexible technology platform [20]. The fabricated switches are measured, and the experimental results successfully compared to simulations, thus validating the design approach. An estimation of the RF behavior of the switches is obtained from 2.5 D electromagnetic simulation. The RF behavior after fabrication is assessed by measuring the switch transmission coefficient for both (ON/OFF) states. Equivalent circuit topologies are also proposed and the value of the circuit elements computed by fitting the simulated results to the measurements. The switch transmission coefficient is also used for the measurement of the switch hysteresis. The proposed switches are integrated into the microwave and mm-wave multimodal reconfigurable circuits to validate the multimodal design approach. Some examples of fabricated multimodal reconfigurable filters and phase switches using RF-MEMS switches with various mechanical topologies (bridge-type featuring ohmic contact and capacitive contact, and cantilever-type featuring ohmic contact) are presented.

This chapter is organized as follows. After this introduction, the multimodal circuits and models for uniplanar transitions and discontinuities are explained in Section 2. The RF-MEMS fabrication technology platform is described in Section 3. The electromechanical analysis derived from the energy approach is studied in Section 4. The fabricated switches are described in Section 5. The RF equivalent circuit for the switches is analyzed in Section 6. The reconfigurable multimodal microwave and mm-wave circuits are described in Section 7. The chapter ends with some conclusions.

2. Uniplanar lines and multimodal models for transitions and discontinuities

2.1. The slotline and the coplanar waveguide

The slotline and the CPW are uniplanar transmission lines. The slotline consists of two conductor strips on a dielectric substrate (**Figure 1(a)**). The CPW consists of three conductor strips on a dielectric substrate (**Figure 1(b)**). The slotline is a monomodal transmission line: it propagates only one fundamental quasi-transversal electromagnetic (TEM) mode, whose voltages and currents (both for the total voltage and current $V_s(z)$ and $I_s(z)$, and for the forward and backward propagating waves $V_s^+(z)$, $I_s^+(z)$, and $V_s^-(z)$, $I_s^-(z)$, respectively) are defined as in **Figure 2(a)** and can be circuitally modeled as an ideal transmission line (**Figure 2(b)**), with

$$V_S(z) = V_S^+(z) + V_S^-(z) \qquad V_S^+(z) = V_S^+ e^{-j\beta_s z} \qquad V_S^-(z) = V_S^- e^{+j\beta_s z}$$
$$I_S(z) = I_S^+(z) + I_S^-(z) \qquad I_S^+(z) = V_S^+(z)/Z_{0S} \qquad I_S^-(z) = -V_S^-(z)/Z_{0S}$$

where Z_{0s} is the characteristic impedance of the slotline mode and β_s its phase constant.

The CPW is a multimodal transmission line: it can propagate two fundamental quasi-TEM modes simultaneously (the even and odd modes) whose voltages and currents are defined as in **Figure 3(a)**. The odd mode is often seen as spurious, and its propagation cut by means of air bridges (described subsequently). However, it can be used to design new kinds of compact uniplanar circuits. In a CPW section, the even and odd modes do not interact between them and therefore can be circuitally modeled as two independent ideal transmission lines, as shown in **Figure 3(b)**, with equations analogous to those of the slotline for either of them.

2.2. Multimodal models for CPW circuits

The even and odd modes behave differently when they encounter any transition or asymmetry, and there they may also interact between them. A multimodal model is a circuit model that makes the behavior of the different modes at a transition or asymmetry explicit. As an
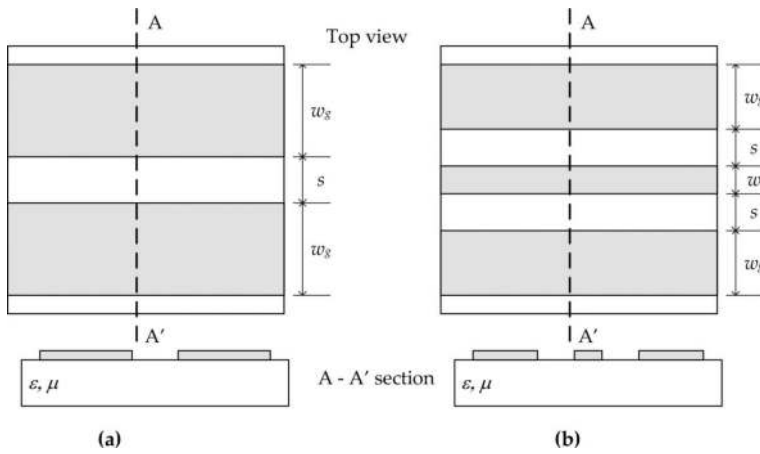
Figure 1. (a) Slotline. (b) CPW.
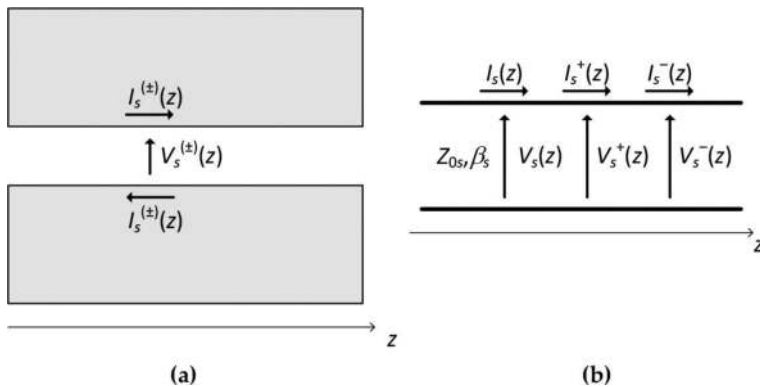
Figure 2. (a) Definitions of voltages and currents in a slotline. (b) Circuit model for a slotline section.

example, some simple multimodal models are presented subsequently; more complex ones are described in [6, 9–11, 38–40, 58].

2.2.1. Symmetric CPW-to-slotline transition

The layout of this transition is shown in **Figure 4(a)** (the depicted voltages and currents are the total ones for each mode, computed at the transition plane). Its behavior is easy to understand intuitively. At the transition, the odd mode transforms into the slotline mode and vice versa due to their similarity of voltage and current orientations (caused by the similarity of their electromagnetic fields). The even mode, however, is left in open circuit when the slotline begins since its current in the CPW central strip can flow no more. Therefore, the multimodal circuit model
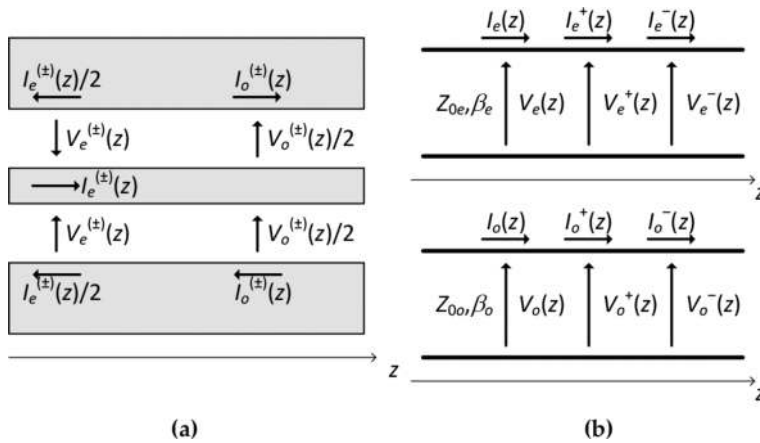

Figure 3. (a) Definitions of voltages and currents in a CPW. (b) Circuit model for a CPW section.
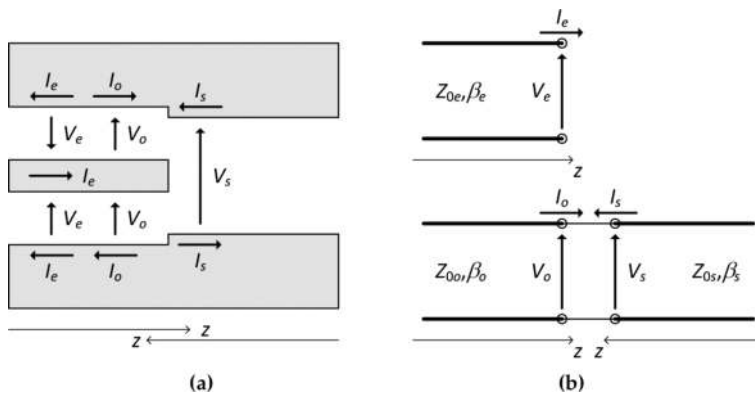

Figure 4. (a) Symmetric CPW-to-slotline transition. (b) Multimodal circuit model.

for the symmetric CPW-to-slotline transition is that of **Figure 4(b)**. As can be seen, a multimodal circuit model confines the contributions of each mode present in a transition into a different port.

2.2.2. Impedances connecting the two outer CPW strips and air bridges

Suppose an impedance connects the two outer CPW strips as shown in **Figure 5(a)**. This circuit can model an air bridge (a conducting wire connecting the two outer CPW strips, with an impedance $Z = 0$ ideally), but also more complicated situations. The even mode does not interact with the impedance since the two outer CPW conductors have the same even-mode electric potential. Therefore, the impedance behaves as a shunt impedance for the odd mode, and it is transparent to the even mode. Thus, its circuit model is that of **Figure 5(b)**. As can be seen, an air bridge ($Z = 0$) blocks the propagation of the odd mode by short-circuiting it. By controlling the value of Z, for instance, by means of MEMS switches, the amount of odd mode that propagates from the left side of the CPW to the right one can be controlled without affecting the propagation of the even mode.

2.2.3. Asymmetric shunt impedances in a CPW

In the two previous examples, the even and odd modes behaved in a different way at the analyzed transitions but did not interact between them due to the symmetry of the transitions. When the transitions are asymmetric, as it is the case for the asymmetric shunt impedances connecting the strips of the CPW shown in **Figure 6(a)**, the modes interact between them. The behavior of this transition is not obvious, but it can be rigorously modeled by the circuit shown in **Figure 6(b)** [37]. As can be seen, in this case, there is an energy balance between even and odd modes (there is a circuit connection between the even- and odd-mode ports), provided that the impedances Z_A and Z_B are different. Again, by controlling the values of Z_A and Z_B by means of MEMS switches, the amount of energy transfer among modes can be controlled. This transition and other described in [38–40] are the base for building multimodal uniplanar reconfigurable circuits [6, 9–11, 58] using MEMS switches.
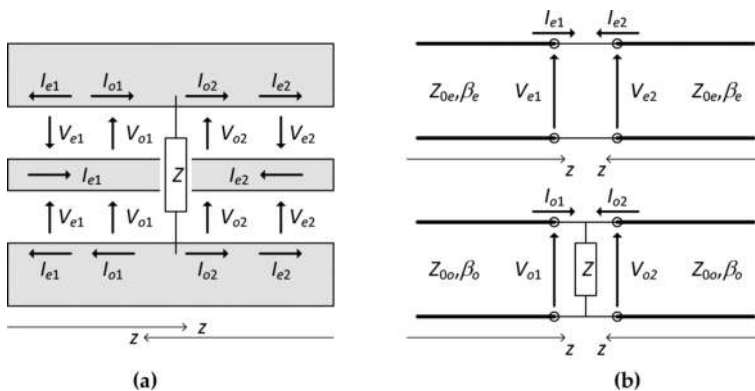

Figure 5. (a) Impedances connecting the two outer CPW strips. (b) Multimodal circuit model.
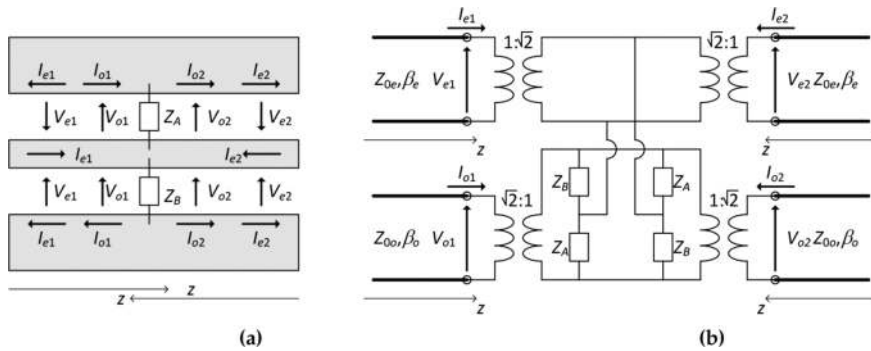
Figure 6. (a) Asymmetric shunt impedances connecting the strips of a CPW. (b) Multimodal circuit model.

3. Fabrication technology for electrostatically actuated RF-MEMS switches

3.1. RF-MEMS technology platform

A flexible technology platform has been developed and optimized at the FBK Institute (Trento, Italy) for the fabrication of RF-MEMS. Basic components (like low-loss CPW, microstrip line and slotline, ohmic [41, 42] and capacitive [43, 44] switches, variable capacitors and inductors) can be integrated in complex reconfigurable RF circuits. Many kinds of devices were produced, mainly for space and communication application, like switching matrices [45, 46], tunable and switchable phase shifters [47], reconfigurable antennas, impedance matching networks [48], VCOs [49, 50], and tunable filters. Depending on the used substrate, high-resistivity silicon (<40 GHz), or fused quartz (>40 GHz), the working frequency range spans from sub-GHz up to more than 100 GHz.

The base process requires eight lithography masks but, depending on the requirements, it can easily be expanded to deposit and pattern metal on the wafer backside to realize microstrip lines or antennas and to obtain devices suspended over thin membranes by locally removing the substrate. A wafer-to-wafer or a cap-to-die-bonding module is also available to encapsulate the delicate MEMS moving parts [51].

RF signal lines and ground area are made of thick electroplated gold to reduce insertion losses while actuation electrodes and DC-bias signal lines are made of a high-resistivity polysilicon to minimize coupling with adjacent RF lines. The movable and suspended structures of the electrostatically actuated switches, which can be either cantilevers or clamped-clamped beams, are made by gold deposited over a sacrificial photoresist layer having the thickness of the required air gap, while switch underpass lines and other conductors are made of a thin Al film. On ohmic-contact switches, the gold-to-gold contact area is defined by underneath polysilicon protruding dimples to ensure a repeatable contact force and a uniform and reproducible low contact resistance. On capacitive-contact switches, the contact capacitor is made by depositing a thin silicon oxide dielectric and an upper floating metal (FLOMET) electrode

over the metal underpass line, obtaining a very well-defined and reproducible metal insulator metal (MIM) capacitor. In this way, when the switch-movable membrane is in an up position, the capacitance, due mainly to the air gap, is small while when it is actuated, the membrane contacts the top floating metal electrode, and the capacitance is defined by the MIM capacitor and not by the membrane itself. In this way, the switch is much more repeatable than the usual configuration, where the movable membrane directly touches the dielectric and the capacitance is strongly influenced by both the membrane deformations and surface roughness leading to a capacitance value much lower than the designed one.

For all the switch configurations, the actuation electrodes are separated from the contact area. This makes it possible to optimize them independently to sustain the high actuation voltage (up to 100 V) and reducing the charging phenomena. It is possible either to use a thicker dielectric over polysilicon to limit the electric field or better to use a dielectric-free configuration removing all the dielectric and using a matrix of mechanical stoppers to prevent short circuits. The height of the stoppers has to be designed in order to obtain an air gap between movable bridges and electrodes which is thick enough for isolation at the bias voltage used.
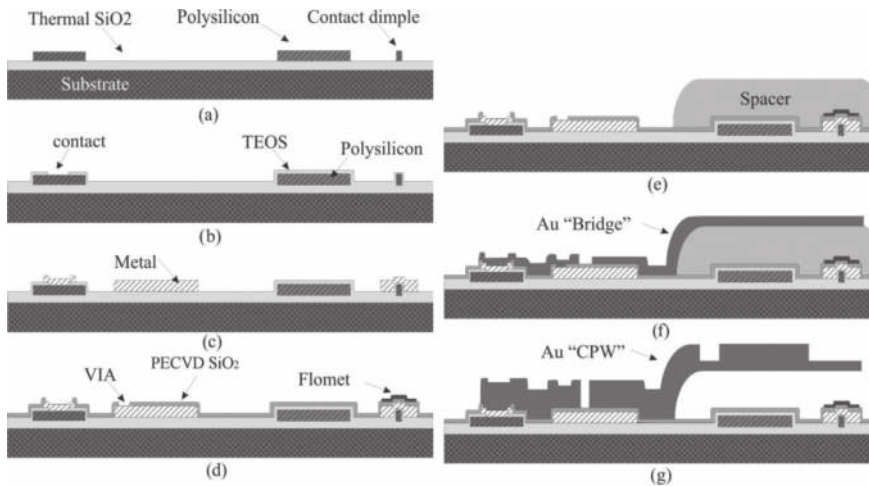
3.2. Fabrication process

The basic fabrication process for silicon substrate is reported in [20, 52] and illustrated in **Figure 7**, where a schematic cross section of an ohmic switch is represented. For high-frequency devices, the losses of the silicon are too high and quartz (fused silica) is preferred. Only minor adjustments are required to process transparent substrates.

The fabrication process starts with the oxidation of the high-resistivity (>5000 Ω·cm) 150-mm diameter silicon wafers in order to obtain a 1-μm-thick silicon oxide isolation layer. A 630-nm thick layer of polysilicon is then deposited by low-pressure chemical vapor deposition (LPCVD) and doped by ion implantation to obtain a sheet resistance of about 1600 Ω/sq. The polysilicon structures are defined by lithography and dry etching using chlorine-based gas plasma, and the residual photoresist is removed by an oxygen plasma (**Figure 7(a)**). An annealing at 925°C for 1 h in nitrogen atmosphere is required to diffuse and to electrically activate the B ions. To electrically isolate the polysilicon, 300 nm of silicon dioxide is deposited by LPCVD at 718°C (TEOS). When a backside conductive layer is required for microstrip lines or devices like phased array antennas, an aluminum film is sputtered and patterned on the wafer backside. The process continues on the front side with a lithography and dry etching to open holes in the TEOS layer for contacting the underneath polysilicon (**Figure 7(b)**). To realize connection lines, a conductive metal consisting of Ti/TiN diffusion barrier and Al1%Si is sputtered and patterned by dry etching (**Figure 7(c)**). The total thickness is the same as that of polysilicon to minimize distortion of the switch bridges crossing over both metal underpass and polysilicon actuation electrodes. A 100-nm thick SiO_2 deposited by PECVD is used as dielectric for capacitive contacts as well as for metal isolation. Holes in the oxide (vias) are realized by lithography and dry etching to contact the underneath metal and for the dielectric-free actuation electrodes (**Figure 7(d)**).

To realize the bottom part of the gold-to-gold contacts of ohmic switches as well as an electrically floating metal layer for capacitive-contact switches, a 5-nm Cr adhesion layer and 150-nm Au are deposited by an electron beam gun, patterned and wet etched (**Figure 7(d)**).

Figure 7. Depiction of the fabrication process flow on a schematic ohmic-switch cross section.

A photoresist sacrificial layer (spacer) is lithographically defined under movable structures and suspended air bridges because later it can be easily removed by oxygen plasma to form an air gap (**Figure 7(e)**). To make the RF structures, a conductive seed layer of 2.5 nm of Cr and 25 nm of Au is deposited by e-beam, patterned using thick AZ 4562 positive resist, and a 1.8-μm-thick first gold layer (bridge) having a slightly tensile residual stress is selectively grown by electroplating (**Figure 7(f)**). A second 3.5-μm-thick gold layer (CPW) is then defined by AZ 4562 and electroplated. The thinner Au bridge layer is used to make the suspended and movable structure while both layers are superimposed to obtain thicker low resistance signal lines and ground areas. To better control the deformation of the movable parts of the switch, it is possible to use the bridge layer for deformable suspension legs and bridge plus CPW layer for a stiffer main body that moves rigidly, almost without deformations. This concept is applied in the fabricated devices, described in Section 5. To complete the fabrication, the seed layer is removed by wet etching, and the suspended structures are released by removing the spacer underneath by an oxygen plasma (**Figure 7(g)**).

4. Electromechanical models for electrostatically actuated RF-MEMS switches: energy considerations

Mechanical design plays an important role in the RF behavior of MEMS switches because it couples important parameters such as the required actuation voltage (also called pull-in voltage, $V_{pull-in}$), actuation time, release time, and the appearance of a bouncing phenomenon after release, which delays a complete release of the switch. The pull-in voltage is commonly calculated assuming a static mechanical behavior in RF-MEMS switches. For compatibility of RF-MEMS with low-voltage CMOS and BiCMOS technologies [14], charge-pump techniques are often used [53]. Nonetheless, a current trend is to decrease the MEMS high $V_{pull-in}$, because charge pump has some limitations given the ever-reducing voltages in CMOS and BiCMOS [54].

One strategy is to dynamically drive the RF-MEMS switches with an input step voltage waveform, which has shown that can decrease the actuation voltage [55]. However, the induced dynamic mechanical behavior can cause an important bouncing phenomenon after release and deeply affect the switch RF/microwave isolation relevant to the RF/microwave behavior, disabling fast-switching applications.

Another trend to achieve fast-switching is to use actuation voltages beyond pull-in. The accumulated electrostatic energy will generate mechanical energy that will be released in the form of mechanical oscillations (bouncing) of the switch membrane [30–35]. To accurately approach RF-MEMS mechanical design, the dynamic behavior of RF-MEMS switches should be considered rather than only static behavior.

The analysis of the electromechanical exchange of energy in the RF-MEMS is an analytical tool that can provide inside knowledge on the required minimum $V_{pull-in}$. It also takes into account the rebound after release due to the increased actuation voltages [26]. During the switching process, the mechanical membrane or the cantilever undergoes an important deformation. To capture this influence, nonlinear terms should be used in the mechanical model [35].

Figure 8 shows the schematic of the one-dimensional (1D) lumped-mass model that, combined with classical Newtonian mechanics, can be used to predict the behavior under applied electrostatic forces of an RF-MEMS switch (either a membrane or a cantilever). If air damping is considered the only non-conservative force, then the equation of the motion for the 1D model shown in **Figure 8** is

$$m_{ef}\ddot{y} + b_{ef}\dot{y} + k_{ef}y = F_o \tag{1}$$

where m_{eff} is the effective mass of the mechanical structure, b_{eff} is the damping coefficient ($= \sqrt{m_{eff}k_{eff}}/Q$, where Q is the mechanical quality factor), $k_{eff} = k_1 + k_3 y^2$, where k_1 and k_3 are the spring constants in the direction of the motion of the mechanical structure, and F_o is the summation of all external forces applied (i.e., the electrostatic force).

The study of the energy exchange of the mechanical system not only provides the position of the contact point of the MEMS switch but also provides deep insight to the required $V_{pull-in}$, the maximum rebound height, and the actual actuation/release times. For the lumped model shown in **Figure 8**, the total energy of the system E is expressed as

$$E = \left(\frac{1}{2}m_{eff}\dot{y}^2\right) + \left(\frac{1}{2}k_1 y^2 + \frac{1}{2}k_3 y^4\right) + \left(\frac{\varepsilon_o A}{2\left(g_i - y\right)^2}V^2\right) \tag{2}$$
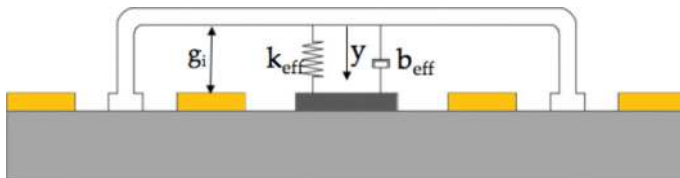
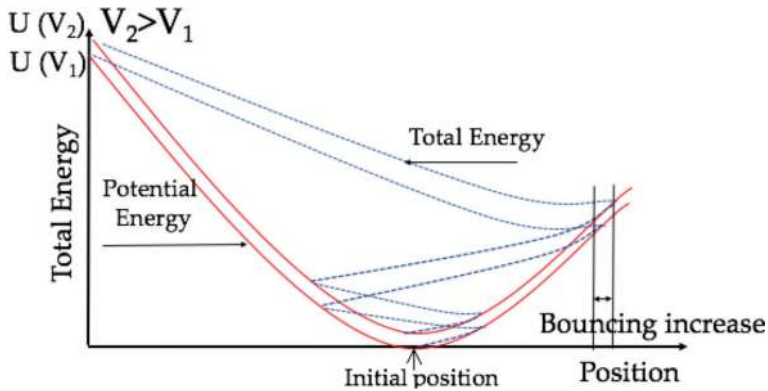**Figure 8.** 1D mechanical lumped-mass model of an RF-MEMS switch.

Figure 9. Simulated evolution of the switch total energy after release from the actuated position.

where V is the applied actuation voltage, ε_0 is the dielectric constant, g_i is the initial gap between the electrodes, and A is the area of the electrodes. In Eq. (2), the first term in brackets is the kinetic energy, the second is the potential energy U_m stored as the mechanical deformation of the structure, and the third is the electrical potential energy U_e. The different thermal processes in the RF switch fabrication (explained in Section 3) can induce an intrinsic residual stress. This effect produces a nonlinear mechanical behavior which can be modeled as a nonlinear spring with spring constants k_1 and k_3.

Figure 9 shows the evolution of the total energy E with respect to the position of the contact point of the mechanical structure along the gap when the switch is released from the actuated position. It can be observed that the total energy E evolves due to inertia and damping forces but is bounded by the potential energy curve ($U = U_m + U_e$), and the change on the potential energy accumulated can modify both the rebounds and the isolation time.

From Eq. (2), the actuation voltage can be obtained since at the point of instability (or switching) $\partial E/\partial y = 0$. In case of nonlinear mechanical behavior, the resulting expression of $V_{pull\text{-}in}$ is as follows:

$$V_{pull\_in} \approx \sqrt{\frac{g_i^{\,3}}{4\,\varepsilon_o\,A}\left(\frac{k_3\,g_i^{\,2}}{8}+k_1\right)} \tag{3}$$

Eq. (3) is used in the simulations of the fabricated switches, discussed in the next Section.

5. Electrostatically actuated RF-MEMS switch configurations for reconfigurable uniplanar circuits

This section presents electrostatically actuated switch configurations which can easily be integrated in reconfigurable uniplanar circuits. All the considered devices were fabricated using the eight-mask surface micromachining process from FBK explained in Section 3. The structures are composed of a 1.8-μm-thick gold layer and reinforced with a 3.5-μm-thick

superimposed gold frame to increase the rigidity of the cantilever or the bridge. The switches were designed taking into account the mechanical analysis described in Section 4.

To reduce the initial deformation of the switch membrane, different authors have reported on the effective stiffness of common suspensions types [26–28]. A coupled-field 3D finite element analysis (FEA) with ANSYS® Workbench™ can be used to model the mechanical structure and tune the measured initial deformation according to the residual stress produced by the fabrication process. The robustness of the design to manufacturing stresses can also be studied with this software.

The switch designs presented use either a clamped-clamped suspension or alternative suspension techniques such as straight-beam, curved-beam, or folded-beam which reduce the initial stress and the actuation voltage. Some FEA results are shown to assess the ability of the proposed suspensions to absorb the initial stress. Hysteresis measurements are also presented to show the featured pull-in and pull-out voltages. At the end of the section, **Table 1** summarizes the switch dimensions and the main mechanical parameters for the different switches.

The RF behavior of the switches, including equivalent circuits in ON and OFF states, is discussed in detail in Section 6.

5.1. Cantilever-type switches for switchable asymmetric shunt impedances

Figure 10 shows a cantilever-type ohmic-contact switch, able to synthesize asymmetric shunt impedances in a CPW to control the CPW even mode as explained in Section 2.2.3. The cantilever is placed above a rectangular notch in the upper lateral ground plane to which is anchored using a suspension composed of two 16-µm-wide beams, providing a low spring constant value and a low pull-in voltage. The beams may be either straight-shaped (**Figure 10(a)**) or semi-circular-shaped (**Figure 10(b)**). The latter is used to reduce the initial deformation of the switch due to the residual stress [27] produced by the fabrication process [20, 52]. To compute the initial deflection, a 3D FEA using ANSYS® was performed. The initial stress values used for the simulation were $\sigma_2 = 58$ MPa (gold layer with a thickness $t_2 = 1.8$ µm) and $\sigma_1 = 62$ MPa (gold layer with a thickness $t_1 = 3.5$ µm). As shown in **Figure 10(c)**, the simulated initial deformation was −0.19 µm. The devices were fabricated on a quartz substrate ($\varepsilon_r = 3.8$) with a thickness $h = 300$ µm and an air gap $g_i = 1.6$ µm. An isolated, high-resistivity polysilicon lower electrode is placed in the notch underneath the cantilever. Three ohmic contacts are defined on the bottom edge, and small dimples (12×10 µm^2) of polysilicon are placed underneath, creating contact bumps to reduce the contact resistance and enhance the RF behavior.

5.2. Bridge-type switches

Bridge-type switches can be used to perform both ohmic contacts and capacitive contacts in uniplanar circuits for multiple applications. In contrast to the cantilever-type switches, the bridge-types are symmetric structures and therefore (as discussed in Section 2.2), when actuated, they are able to control one of the fundamental CPW modes (either even or odd), leaving the other mode ideally unaffected. Some minor effects such as a small even-mode parasitic

Parameter	Ohmic-cantilever straight/semicircle	Capacitive, clamped/folded	Ohmic-series	Ohmic-parallel (SAB)
Figure	10(a)/10(b)	11(a)/11(b)	13(a)	14(a)
Supporting beam radius (μm)	–/16	—	—	—
Meander length, a (μm)	—	–/30	—	30
Supporting beam width (μm)	16	–/10	—	10
Supporting beam length, b (μm)	40	–/75	—	75
Supporting beam length, e (μm)	—	–/45	—	77.5
Membrane width, c (μm)	90	90	100	90
Window width, d (μm)	—	—	—	60
Membrane length, f (μm)	170	580/230	580	165
Bottom electrodes area (μm²)	13,500	2 × 22,800/2 × 7650	2 × 22,800	2 × 7650
Contact area (μm²)	3 × 10 × 30	100 × 90[*]/50 × 90[*]	2 × 10 × 90	2 × 10 × 12
Spring constant, $keff$ (N/m)[‡]	2.3/1.6	104.5/32.5	104.5	15.4
Pull-in voltage, $Vpull\_in$ (V)[†]	10.6/8.8	60/14	49	14
Resonant frequency (KHz)	8[‡]/6.6[‡]	16.25 [‡]/25.3[‡]	16.25[†,‡]	17.1[‡]

[†]Measured.

[‡]Calculated using the mechanical analysis of Section 4.

[*]Floating metal area.

Table 1. Dimensions and mechanical parameters of the switches.

capacitance (in case of the ohmic-contact parallel switch discussed in Section 5.2.3) occur but with a very limited impact on the circuit behavior.

5.2.1. Capacitive-contact parallel switch

Figure 11 shows two fabricated capacitive-contact parallel switches. The change between ON and OFF states is performed by moving the suspended membrane, which can be actuated through bias pads connected to two symmetrical polysilicon electrodes placed under the membrane. A floating metal (FLOMET) strip is placed on top of the dielectric under the membrane. The overlapping area between FLOMET and a multi-metal layer under the bridge (CPW center conductor) defines a MIM capacitor, as described in Section 3. When the actuation voltage is equal or higher than the pull-in voltage V_{pull_in}, the bridge collapses on the FLOMET, producing a reproducible, constant-value down-state capacitance. The resistance of the ohmic contact between the membrane and the FLOMET strip fixes the amount of switch
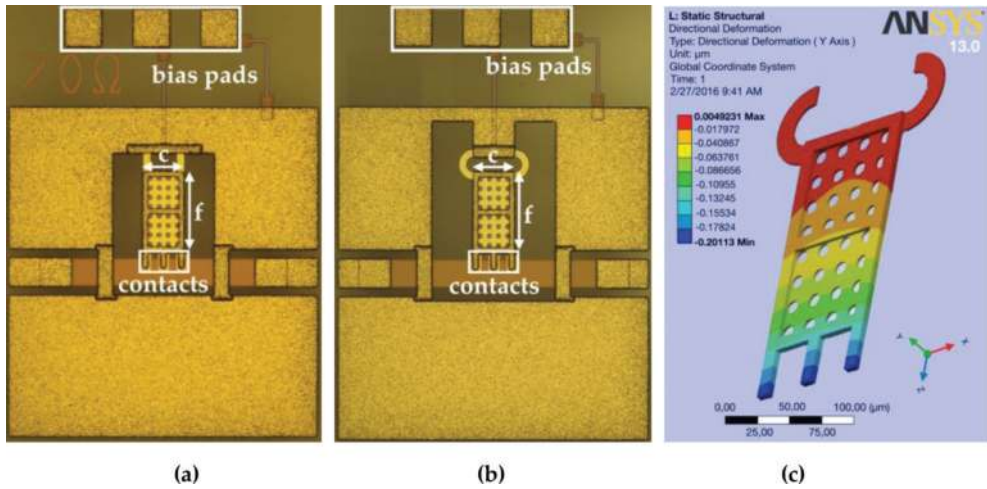
Figure 10. Cantilever-type ohmic-contact switch. (a) Straight-shaped suspension. (b) Semi-circular-shaped suspension. (c) Simulation of initial deformation due to residual stress on the semi-circular suspension device.
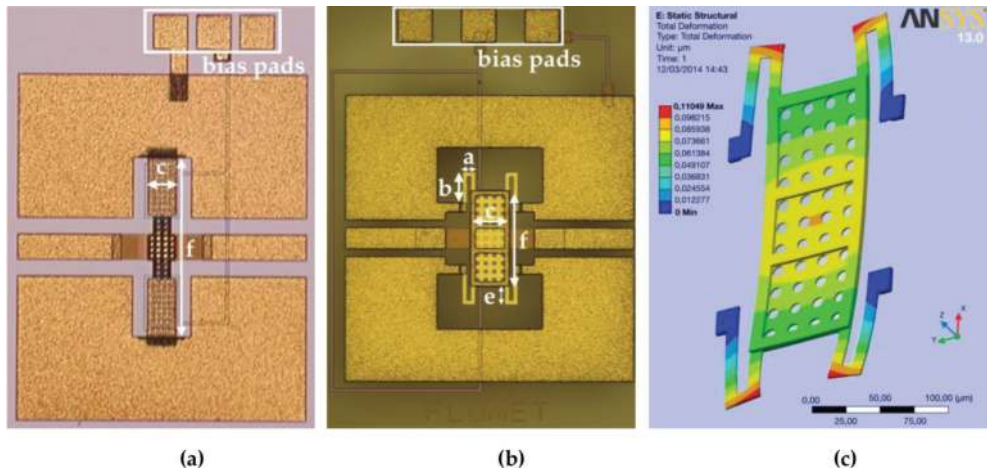
Figure 11. Capacitive-contact parallel switch. (a) Fabricated switch using a clamped-clamped membrane. (b) Fabricated switch using a folded-beam suspension. (c) for a device with a folded-beam suspension: Simulation of initial deformation due to residual stress.

RF insertion loss. The MIM capacitor combined with the membrane inductance defines an RLC circuit in the down state. The RF equivalent circuit details are given in Section 6.

The capacitive switch shown in **Figure 11(a)** uses a clamped-clamped membrane suspension. The device was fabricated on a quartz substrate with a thickness $h = 500$ μm and an air gap $g_i = 2.7$ μm. The area of each actuation electrode is 120×190 μm². The MIM capacitor area is 90×100 μm², which gives a capacitance of 3.8 pF. The capacitive switch of **Figure 11(b)** uses a folded-beam suspension. It was fabricated on a quartz substrate with a thickness $h = 300$ μm

and an air gap g_i = 1.6 µm. Each actuation electrode has an area of 90 × 85 µm². The MIM capacitor area is 90 × 50 µm², which gives a capacitance of 1.5 pF (without taking into account the fringing fields) calculated, as with the previous switch, using 2.5-D planar-simulation software. As with the cantilever switch shown in **Figure 10(b)**, the deformation of the bridge due to stress gradients was simulated using ANSYS® 3D FEA. As shown in **Figure 11(c)**, the maximum initial deflection is 0.11 µm. The simulated stiffness constant is k_{eff} = 32.5 N/m, and the calculated pull-in voltage is V_{pull_in} = 15.6 V. **Figure 12** shows the measured hysteresis of the switch. The measured pull-in voltage when the isolation is higher than 12 dB at 10 GHz is V_{pull_in} = 14 V.
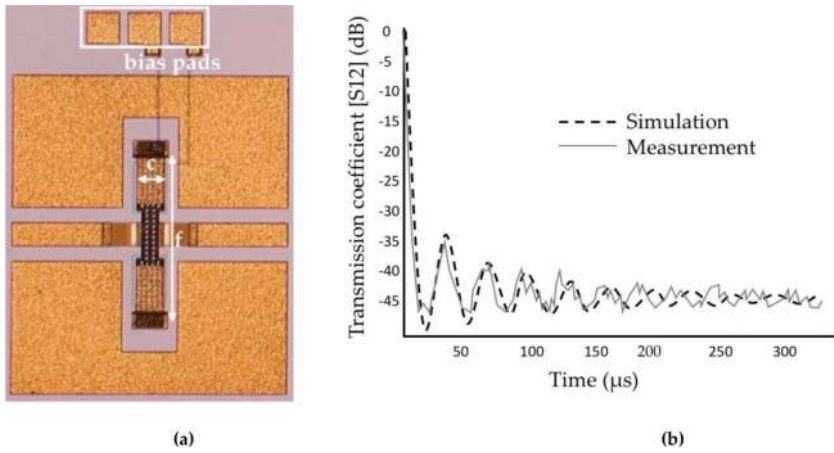
5.2.2. Ohmic-contact series switch

A photograph of an ohmic-contact series switch is shown in **Figure 13(a)**. It was fabricated on a quartz substrate with a thickness h = 500 µm and an air gap g_i = 2.7 µm The CPW line does not have continuity under the membrane. When the membrane is in its up state, the switch is OFF, while when the membrane is in a down state, the switch is ON, since the metallic membrane puts into contact the two sides of the CPW line. Two electrodes are placed under the membrane at both sides to generate the actuation force. The area of each actuation electrode is 120 × 190 µm². As with the previous switches, the bias pads are isolated from the membrane using thin high-resistivity silicon bias lines.

For this switch, the switching and release times were key parameters in radiometric applications, as discussed in Section 7. The measured switching and release times are 100 µs and 15 µs, respectively. To more accurately assess the switch behavior after the membrane release (evolving from ON state to OFF state), the energy model discussed in Section 4 was applied as follows. The evolution in time of the switch transmission coefficient magnitude $|s_{21}(t)|$ (isolation) at a given RF frequency (f = 3 GHz) was measured after removing the applied actuation voltage. Then, from the energy equation (Eq. (2)), which can be solved numerically, the evolution of the capacitance $C(y_r)$ was calculated. Next, using the equivalent circuit for this particular switch design (**Figure 18(a)**), the switch transmission coefficient magnitude as a function
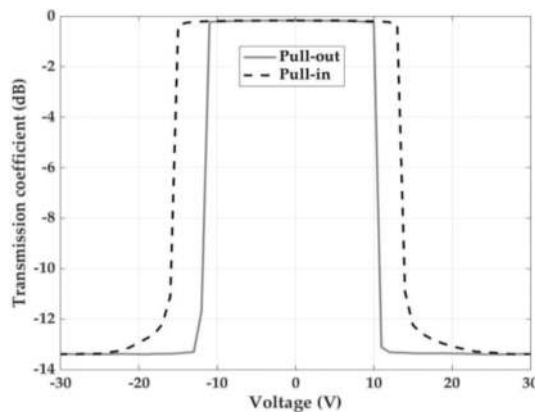
Figure 12. Measurement of hysteresis of the switch with a folded suspension (**Figure 11(b)**) showing pull-in and pull-out traces.

Figure 13. Ohmic-contact series switch. (a) Fabricated switch. (b) Measured and simulated time evolution of the microwave isolation after release (switch going from ON state to OFF state).
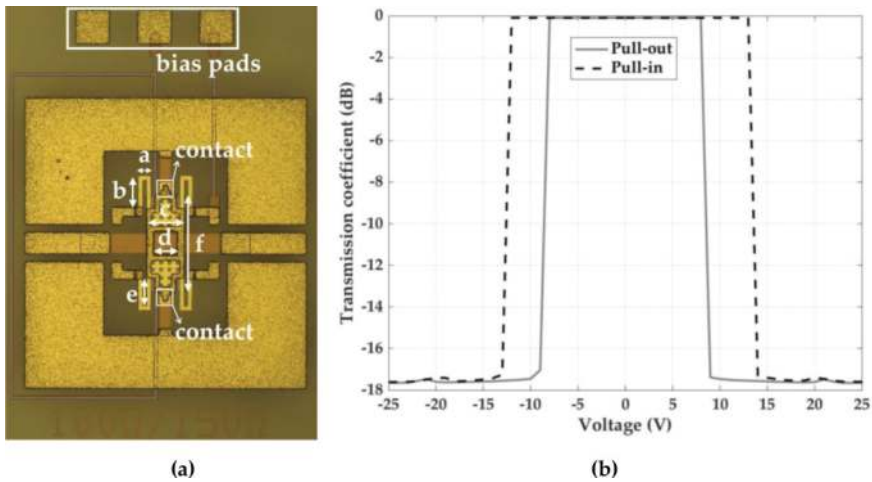
Figure 14. Ohmic-contact parallel switch (switchable air bridge) using a folded-beam suspension. (a) Fabricated switch. (b) Measurement of hysteresis showing pull-in and pull-out traces.

of frequency $|S_{21}(f)|$ was computed which, assuming no parasitic effects ($L_p = 0$ and $C_p = 0$) and no inner line sections, is expressed as

$$|S_{21}(f)| = \frac{4\pi Z_0 f C(y_r)}{\sqrt{1 + \left(4\pi Z_0 f C(y_r)\right)^2}} \tag{4}$$

where Z_0 is the reference impedance and f is the RF frequency. **Figure 13(b)** compares the simulated evolution of $|S_{21}(t)|$ calculated using Eq. (4) (particularized at $f = 3$ GHz) to the measured $|S_{21}(t)|$ for the series ohmic-contact switch shown in **Figure 13(a)**, showing a good agreement.

5.2.3. Ohmic-contact parallel switch (switchable air bridge)

Figure 14(a) shows a switchable air bridge (SAB) that can be used in CPW reconfigurable multimodal circuits for a selective use of the CPW odd mode. The device was fabricated on a quartz substrate with a thickness h = 300 μm and an air gap g_i = 1.6 μm. The structure features a reinforced gold membrane with two ohmic contacts at the edges. The bridge membrane is anchored to isolated islands by folded-beam suspensions, made of a 1.8-μm-thick, 10-μm-wide single gold layer. When an actuation voltage equal or higher than the pull-in voltage V_{pull_in} is applied, the bridge collapses over an underpass metal layer connected to the ground planes of the CPW. The SAB has an air gap of 1.6 μm, and the distance between the membrane and the bottom ohmic contacts over the underpass metal layer is 1.3 μm. The measured hysteresis of the ohmic switch is shown in **Figure 14(b)**. The pull-in voltage was measured when the isolation is higher than 17 dB at 10 GHz. The measured pull-in voltage is V_{pull_in} = 14 V, and the simulated stiffness constant is k_{eff} = 15.4 N/m. The first-mode mechanical resonant frequency f_{0m} = 17.1 kHz was obtained from the electromechanical analysis (ANSYS®).

The air gap of ohmic contacts placed on the top and bottom electrodes could be affected by stress gradients during fabrication. As with the previous switches, the deformation of the bridge was simulated using ANSYS® 3D FEA. The structure can handle positive- and negative-stress gradients without compromising on the function of the switch. **Figure 15(a)** shows the deformation of the bilayer membrane. For this case, the simulated maximum initial deflection is smaller than 0.16 μm.

The measured topography of the device just after fabrication (**Figure 15(b)**) shows a very good agreement with the 3D FEA results, thus validating this analysis. This model can then be used to extract the nonlinear stiffness values that in turn can modify the potential energy curve shown in **Figure 9**.
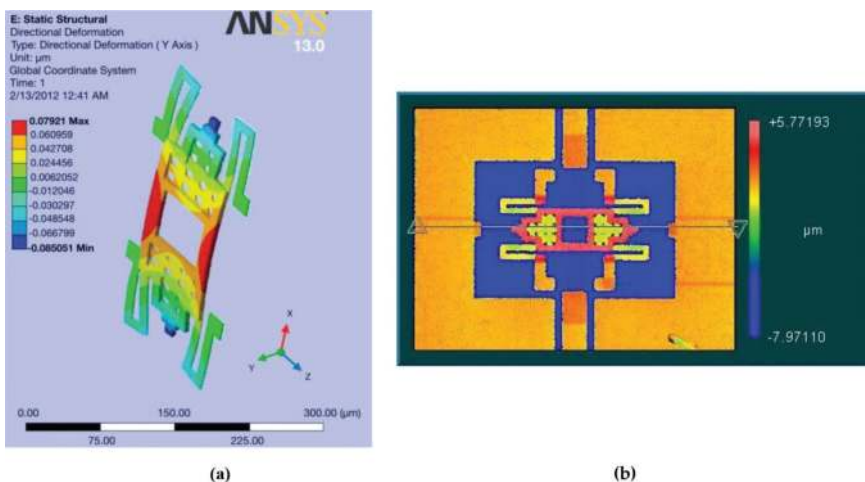
Figure 15. (a) Initial deformation due to residual stress. (b) Measured topography of the device just after fabrication.

Table 1 shows the dimensions and the main mechanical parameters of the switches presented in this section. The membrane/cantilever height is 1.6 μm in all cases except for the capacitive-contact parallel switch with the clamped-clamped membrane and the ohmic-contact series switch, both featuring a membrane height of 2.7 μm. While the pull-in voltages are measured, the spring constant and the mechanical resonant frequency are computed using the 3D FEA method presented in Section 4. For the ohmic-contact series switch, the mechanical resonant frequency was also measured using the method reported in [56].

6. RF-MEMS switch electrical modeling and characterization

6.1. Parallel and series switch models

6.1.1. Capacitive-contact parallel switch

The configuration of a capacitive-contact parallel switch is shown in **Figure 11**. It is able to control the propagation of the CPW even mode and simultaneously suppress the CPW odd mode because the lateral metal planes are permanently connected through the switch membrane. When the switch is in its "up" (OFF) state, the capacitance between the elevated membrane and the RF line underneath (C_{OFF}) is very small. When a bias voltage greater than the pull-in voltage is applied between the membrane and the lower electrodes, the membrane moves down and gets in contact with the floating metal deposited on top of the RF line, implementing the switch "down" (ON) state. In this case, the switch capacitance (C_{ON}) is that of the parallel-plate capacitor defined between the floating metal pad and the underneath RF line section, across a thin oxide layer. The thinner the oxide layer and the larger the overlapping area between the floating metal and the RF line, the larger is the ON capacitance C_{ON}. Thus, the device acts as a switched capacitance. For a highly efficient switch, it is desired to have a high capacitance ratio C_{ON}/C_{OFF}.

Figure 16 shows an equivalent circuit of the switch, which applies to both states. Capacitance C accounts for the switched capacitance and adopts two possible values, C_{ON} and C_{OFF}. The resistance R_C and inductance L_C are membrane resistance and inductance, respectively, at either side of the capacitive contact. The RF frequency at which the switch presents a maximum insertion loss in its ON state is given by the approximate expression $f_0 = (1/\pi) \cdot \sqrt{2 \cdot L_C \cdot C_{ON}}$.
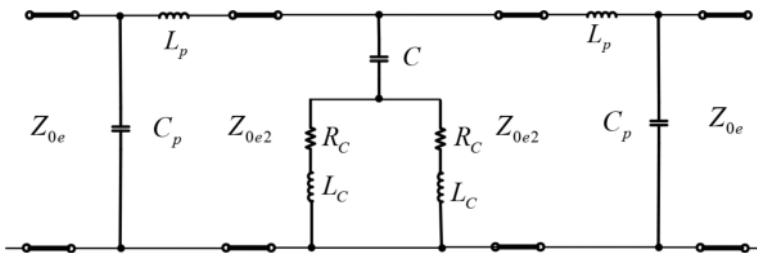
Figure 16. Capacitive-contact parallel-switch equivalent circuit.

A proper combination of the switch ON capacitance C_{ON} and inductance L_C is selected to yield the desired operating frequency f_0 and membrane dimensions for a given fabrication technology. Short even-mode CPW transmission line sections are considered at each side of the membrane, with characteristic impedances Z_{0e} and Z_{0e2} which depend on the CPW line and slot dimensions. The inductance L_p and capacitance C_p are modeling the small parasitic effects due to changes in the width of the CPW central strip and lateral ground planes and can be obtained by adjusting their values to fit a 2.5 D electromagnetic simulation of the CPW structure. The CPW propagation constant and characteristic impedance are also obtained from the electromagnetic simulation of a straight CPW line section of the same dimensions excited with a CPW even mode.

6.1.2. Parallel and series ohmic-contact switches

The configuration of an ohmic-contact parallel switch (switchable air bridge or SAB) is shown in **Figure 14**. This switch is used to efficiently control the CPW odd-mode propagation. When the switch is in its "up" (OFF) state, the capacitance between the elevated membrane and the two RF ohmic contacts at either lateral metal plane is negligible ($C=C_{OFF} < 1$ fF) because the overlap area for contacts is extremely small. When a bias voltage greater than the pull-in voltage is applied between the membrane and the lower electrodes, the membrane moves down and the two edges get in contact with the lateral metal planes, implementing a "bridge" which performs a double ohmic contact (switch "down"—ON—state). The membrane has a window in the center part to reduce the capacitance between the membrane and the central CPW strip, in such a way to minimize the impact on the propagation of the CPW even mode. This capacitance, obtained from measurement, is 47 fF.

Figure 17 shows an equivalent circuit of the switch for the OFF state (**Figure 17(a)**) and ON state (**Figure 17(b)**). The same parasitic inductance L_p and capacitance C_p as in the circuit of **Figure 16** can be observed, but will certainly have different values because they are now modeling the CPW odd mode. The CPW line sections now refer to the CPW odd mode with
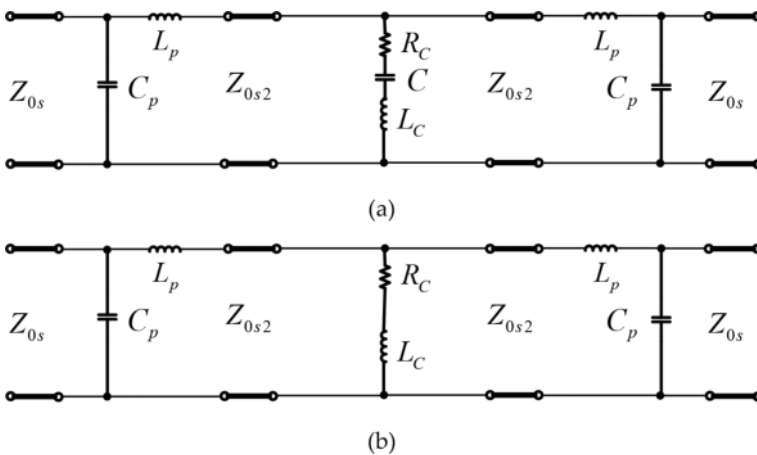

Figure 17. Ohmic-contact parallel-switch equivalent circuit. (a) OFF. (b) ON.
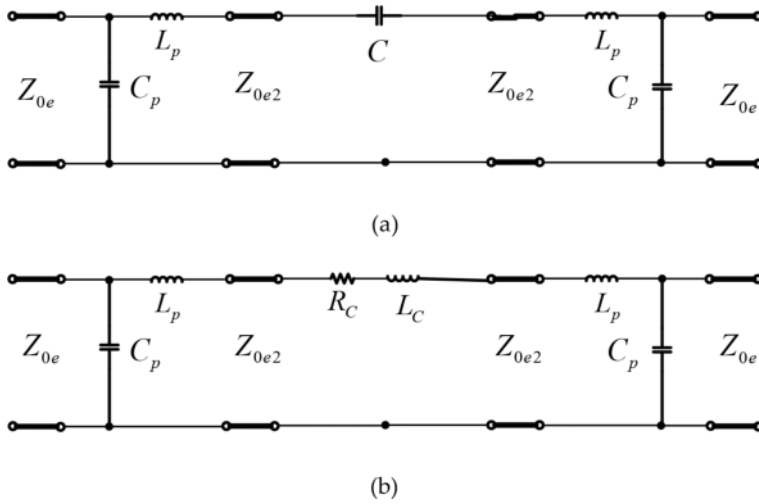
Figure 18. Ohmic-contact series-switch equivalent circuit. (a) OFF. (b) ON.
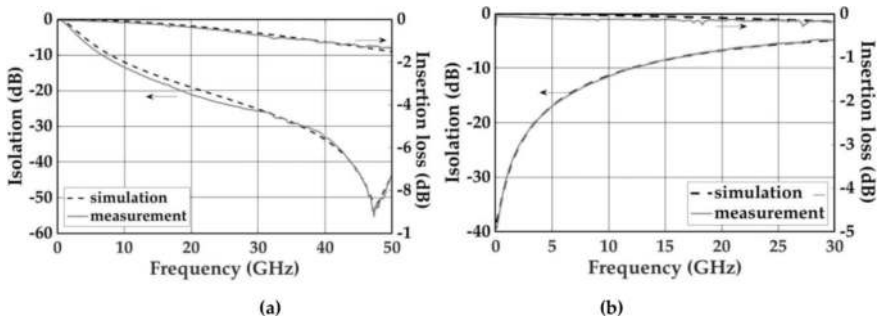

Figure 19. Measured isolation (OFF) and insertion loss (ON) of the fabricated switches compared to simulations of circuit models. (a) Capacitive-contact parallel switch shown in **Figure 11(b)** (model in **Figure 16**). (b) Cantilever-type ohmic-contact parallel switch shown in **Figure 10(a)** (model in **Figure 17**).

characteristic impedances Z_{0s} and Z_{0s2} which depend on the CPW line and slot dimensions. For both states, we consider the same membrane resistance R_C and inductance L_C. In OFF state, the capacitance C_{OFF} between the elevated membrane and the two RF ohmic contacts is taken into account, although its effect is almost negligible.

To control the CPW even-mode propagation using ohmic-contact switches, the cantilever-type switch configuration shown in **Figure 10** can be used. It is observed that the odd mode is suppressed using air bridges. Therefore, the equivalent circuit for this kind of switches is the same as the one shown in **Figure 17**, but changing the CPW line characteristic impedances Z_{0s} and Z_{0s2} with Z_{0e} and Z_{0e2}, respectively. If the two air bridges were removed, the CPW line is able to propagate the CPW odd mode simultaneously to the even mode. In this case, the cantilever-type switch configuration can be used to generate the CPW odd mode whenever

the switch is in its ON state. This structure is favorably used in reconfigurable multimodal filters, as explained in Section 7.2.

The CPW even mode can be controlled without suppressing the odd mode by using the bridge-type ohmic-contact series switch configuration shown in **Figure 13**. In this case, the equivalent circuit for the even mode is shown in **Figure 18**. In the OFF state, the switch behaves as a small series capacitance ($C = C_{OFF} \approx 6$ fF), and it can be described as a series R-L circuit in the ON state.

6.2. Experimental characterization

Figures 19 and **20** compare the measured to simulated results of the switches presented in Section 5 and modeled in Section 6.1. The switch insertion loss (ON state) and isolation (OFF state) are plotted as a function of frequency.
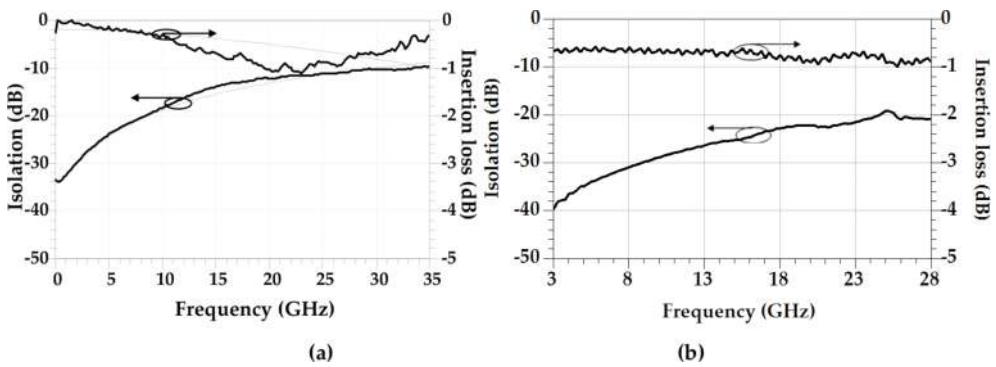
Figure 20. (a) Measured isolation (OFF) and insertion loss (ON) of the fabricated ohmic-contact parallel switch (SAB) shown in **Figure 14(a)** compared to simulations using the circuit model shown in **Figure 17**. (b) Measured isolation (OFF) and insertion loss (ON) of the fabricated bridge-type ohmic-contact series-switch shown in **Figure 13(a)**.

Parameter	Capacitive: direct clamp/folded		Ohmic: parallel		Ohmic: cantilever		Ohmic: series	
	OFF	ON	OFF	ON	OFF	ON	OFF	ON
L_p (nH)	0	0	0	0	0.02	0.02	0	0
C_p (fF)	8.5	8.5	3	3	0	0	6	6
L_C(pH)	28 / 7	28 / 7	180	180	100	100	0	230
C (fF)	1 / 30.5	3800 / 1530	0.9	–	5.1	–	3.35	–
R_C (Ω)	0.27 / 0.1	0.27 / 0.1	0.3	3.2	0	1	0	2.4
Z_{0x} (Ω)*	76.1 / 78.6	76.1 / 78.6	100	100	45.3	45.3	97	97
Z_{0x2}(Ω)*	118.7 / 148.5	118.7 / 148.5	195	195	63.5	63.5	152	152

*x = e (even) or o (odd) according to **Figures 16–18**.

Table 2. Equivalent circuit elements of **Figures 16–18** (switches **Figures 10**, **11**, **13**, and **14**).

In **Table 2**, the values of the equivalent circuit elements obtained to fit measurement are listed. The capacitive switch features a high capacitance ratio ($C_{ON}/C_{OFF} = 50.2$). The ohmic switches feature low insertion loss (<1 dB) and high isolation (>20 dB) for f < 10 GHz (parallel switch) and for f < 25 GHz (series switch).

7. Design of multimodal reconfigurable microwave and mm-wave circuits

This section presents two applications of the RF-MEMS presented in Section 5 when combined with the multimodal circuits presented in Section 2: 180° phase switches and bandpass filters. All of them were fabricated using the process described in Section 3.

7.1. Phase switches

A 180° phase switch is a circuit that shifts the phase between 0 and 180°. This is a multi-purpose element required in the microwave and millimeter-wave applications, such as high-sensitivity radiometers or electronic beam steering in phased-array antennas. The specifications for these systems are, in most cases, a broadband operation, a low power consumption, and small size. They can be implemented monolithically using HBT/HEMT-based MMICs or using MEMS-based solutions as shown subsequently.

Figure 21(a) shows a compact, uniplanar 180° phase switch fabricated on a quartz substrate [9]. It is based on two different back-to-back (BTB) CPW-to-slotline transitions [39] (symmetric and antisymmetric transitions, respectively), creating two phase paths with a relative transmission phase shift between them of 180°. Each path is selected using two single-pole-double-throw (SPDT) switches. The SPDT consists of two ohmic-contact MEMS series switches
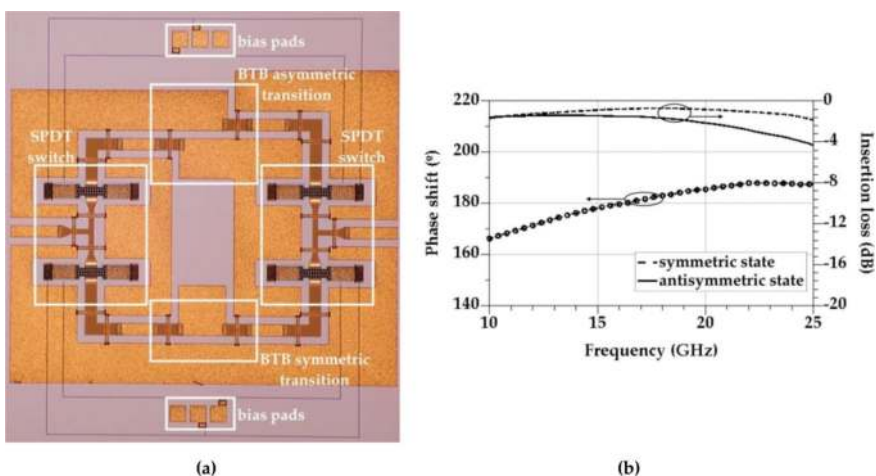
Figure 21. (a) Manufactured 180° phase switch. (b) Measured insertion loss (symmetric and antisymmetric paths) and measured phase shift between the two paths.

(described in Section 5.2.2) and a power divider. **Figure 21(b)** shows the measured performance of the circuit, featuring a 180° ± 5° phase shift between both states in a bandwidth of 35% (14–20 GHz), with an insertion loss smaller than 2 dB in both paths.

Figure 22(a) shows the photograph of a second compact, uniplanar 180° phase switch fabricated on a quartz substrate [10]. In this case, it is based on an air-bridged CPW cross [57]. The two CPW arms of the cross are loaded with capacitive-contact MEMS switches (described in Section 5.2.1). The two phase-switch states (0°/180°) are obtained by actuating the MEMS switches in opposite states (ON/OFF and OFF/ON), resulting in a multimodal interaction between the two CPW modes (even and odd) at the air-bridged cross. The CPW-to-slotline transition [39] at the input port and the CPW taper at the output port are included in order to enable the measurement of the circuit with a probe station. **Figure 22(b)** shows the measured results of phase shift between both states and insertion loss, featuring 180° +1.8°/−1° and ± 0.1 dB insertion-loss unbalance, respectively, in a very wide bandwidth (5–25 GHz). The measured insertion loss is better than 2 dB in 10–20-GHz frequency band.

7.2. Uniplanar bandpass filters

Figure 23(a) shows a second-order bandwidth-reconfigurable bandpass filter, which was fabricated on a quartz substrate ($h = 500$ μm) [11]. The $\lambda_o/2$ slotline resonators are coupled by a slotline short-circuit (K_{12}). The filter features multimodal immittance inverters (MIIs) based on CPW-to-slotline transitions [37, 58] which are embedded in the input and output slotline resonators. As shown in **Figure 23(b)**, two cantilever-type ohmic-contact MEMS switches (described in Section 5.1) are used to enable reconfigurable MIIs. When actuated, the switches modify the input and output coupling of the filter (K_{01} and K_{23}), resulting in a change in the filter's fractional bandwidth (FBW). To keep the central frequency constant, another cantilever MEMS switch (also shown in **Figure 23(b)**) is integrated in K_{12} and actuated simultaneously. **Figure 23(c)** shows the filter measured results. It features two FBW states of 0.082 (when the inner switches are actuated) and 0.043 (when the outer switches and the impedance inverter switch are actuated), while maintaining a constant center frequency (18.9 GHz).

Figure 24(a) shows a second-order bandpass filter fabricated on a 5-KΩ-cm high-resistivity silicon substrate ($\varepsilon_r = 11.9$, $h = 200$ μm), which uses switchable air bridges or SABs [6] (shown in **Figure 24(b)**) similar to the SAB of **Figure 14(a)**. The SABs are described in Section 5.2.3. Like
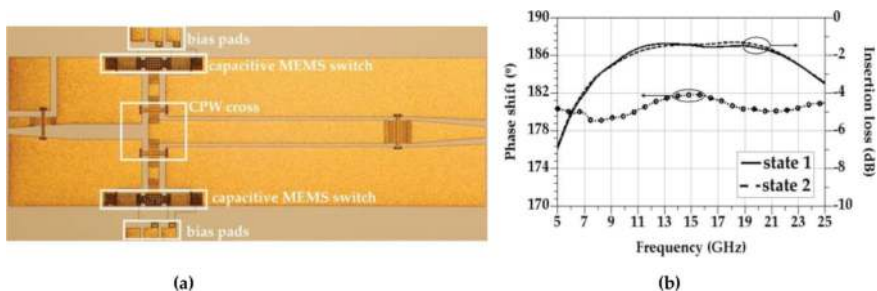
Figure 22. (a) Manufactured 180° phase switch. (b) Measured insertion loss for the two states and phase shift between the two states.
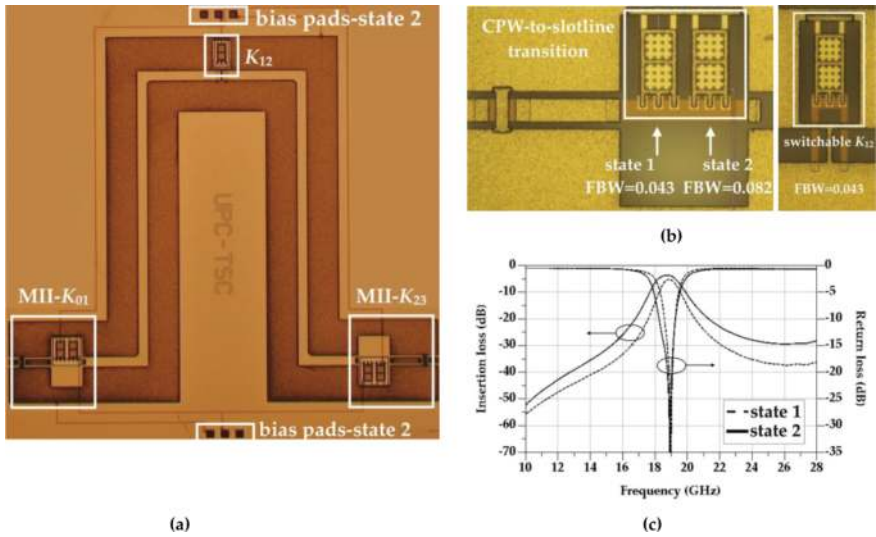
Figure 23. (a) Second-order bandwidth-reconfigurable bandpass filter. (b) Detail of reconfigurable MIIs and reconfigurable inductive coupling K_{12}. (c) Filter measured insertion loss and return loss.
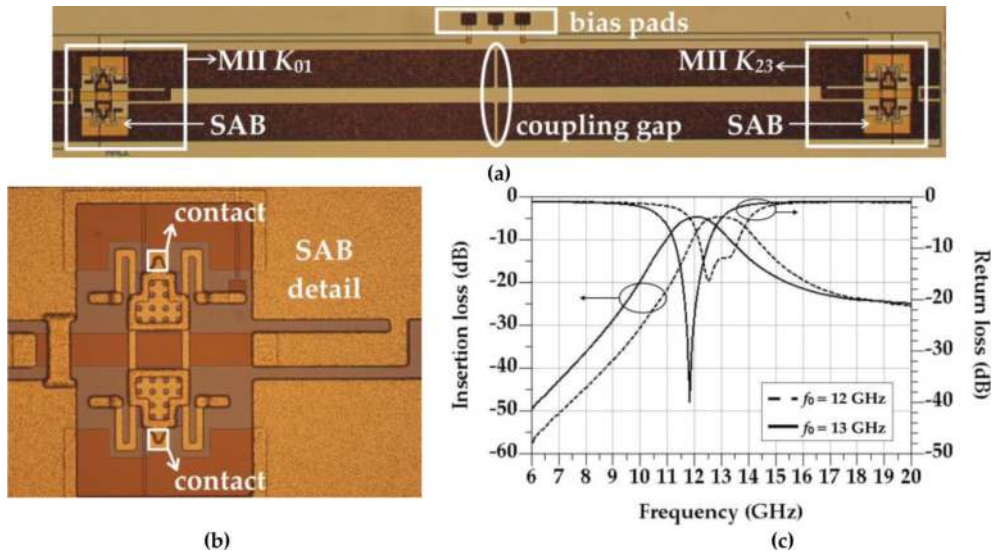

Figure 24. (a) Second-order frequency-reconfigurable bandpass filter. (b) Detail of reconfigurable MIIs and SAB. (c) Filter measured insertion loss and return loss.

the previous example, the filter is fed by reconfigurable MII structures with embedded CPW-to-slotline transitions but uses quarter-wavelength resonators coupled by a slotline gap. When actuated, the SABs reduce the resonators' effective length, which in turn increases the resonance frequency. As a result, the filter center frequency is shifted up. **Figure 24(c)** shows the

filter measured results. It features two operating frequencies, f_0 = 12 GHz and f_0 = 13 GHz, with a constant fractional bandwidth (FBW) of 14%. The measured filter IL is 4.6 dB in both states.

8. Conclusion

In this chapter, the design considerations of RF-MEMS switches aimed to be integrated in uniplanar multimodal reconfigurable circuits for operation in the microwave and mm-wave bands have been presented. Different configurations of series and parallel switches featuring ohmic and capacitive contact have been discussed in detail, including the analysis of mechanical topologies which minimize the initial deformation due to residual stress. The fabrication process has been described, which provides the required flexibility to integrate the MEMS switches into higher-level RF communication systems. The switch RF behavior has been modeled using suitable equivalent circuits for both (ON/OFF) switch states. The models can easily be embedded into complex multimodal environments which enable multipurpose, compact designs. The fabricated switches have been experimentally characterized in terms of hysteresis, RF isolation (OFF state), and RF insertion loss (ON state), demonstrating an excellent behavior. As practical examples of the application into communication systems, some of the proposed switches have successfully been integrated into 0°/180° phase switches and into reconfigurable filters with either center frequency or fractional-bandwidth reconfiguration, showing excellent performances.

Acknowledgements

Author details

Lluis Pradell[1]*, David Girbau[2], Miquel Ribó[3], Jasmina Casals-Terré[4], Antonio Lázaro[2], Adrián Contreras[1], Marco Antonio Llamas[1], Julio Heredia[1], Flavio Giacomozzi[5] and Benno Margesin[5]

*Address all correspondence to: pradell@tsc.upc.edu

1 Department of TSC, Technical University of Catalonia (UPC), Barcelona, Catalonia, Spain

2 Department of EEEA, Rovira i Virgili University, Tarragona, Catalonia, Spain

3 Department of ET, La Salle-Ramon Llull University, Barcelona, Catalonia, Spain

4 Department of EM, UPC, Barcelona, Catalonia, Spain

5 Fondazione Bruno Kessler, Trento, Italy

References

[1] Bakri-Kassem M, Mansour RR. High power latching RF MEMS switches. IEEE Transaction on Microwave Theory and Techniques. 2015:222-232. DOI: 10.1109/TMTT.2014.2376932

[2] Girbau D, Pradell L, Lázaro A, Nebot A. Electrothermally-actuated RF-MEMS switches suspended on a low-resistivity substrate. IEEE/ASME Journal of Microelectromechanical Systems. 2007:1061-1070. DOI: 10.1109/JMEMS.2007.904744

[3] Mennai A, Bessaudou A, Cosset F, Guines C, Passerieux D, Blondy P, Crunteanu A. High Cut-off Frequency RF Switches integrating a Metal-Insulator Transition Material. In: IEEE MTT-S Int. Microwave Symposium; May 2015; Phoenix. New York: IEEE. pp. 1-3

[4] DiNardo S, Farinelli P, Giacomozzi F, Mannocchi G, Marcelli R, Margesin B, Mezzanotte P, Mulloni V, Russer P, Sorrentino R, Vitulli F, Vietzorreck L. Broadband RF-MEMS based SPDT. In: 36th European Microwave Conference; September 2006; Manchester. New York: IEEE. pp. 1727-1730

[5] Ocera A, Farinelli P, Cherubini F, Mezzanotte P, Sorrentino R, Margesin B, Giacomozzi F. A MEMS-Reconfigurable Power Divider on High Resistivity Silicon Substrate. In: IEEE/MTT-S International Microwave Symposium; May 2007; Honolulu. pp. 501-504

[6] Contreras A, Casals-Terré J, Pradell L, Giacomozzi F, Iannacci J, Ribó M. A Ku-band RF-MEMS frequency-reconfigurable multimodal bandpass filter. International Journal of Microwave and Wireless Technologies. 2014:277-285. DOI: 10.1017/S1759078714000567

[7] Cazzorla A, Sorrentino R, Farinelli P. Double-actuation extended tuning range RF MEMS Varactor. In: 45th European Microwave Conference; September 2015; Paris. pp. 937-940

[8] Vähä-Heikkilä T, Varis J, Tuovinen J, Rebeiz GM. A reconfigurable 6-20 GHz RF MEMS impedance tuner. In: IEEE MTT-S International Microwave Symposium; June 2014; Fort Worth. New York: IEEE. pp. 729-732

[9] Llamas MA, Girbau D, Ribó M, Pradell L, Lázaro A, Giacomozzi F, Margesin B. MEMS-based 180° phase switch for differential radiometers. IEEE Transaction on Microwave Theory and Techniques. 2010:1264-1272. DOI: 10.1109/TMTT.2010.2045558

[10] Llamas MA, Girbau D, Ribó M, Pradell L, Giacomozzi F, Colpo S. RF-MEMS uniplanar 180° phase switch based on a multimodal air-bridged CPW cross. IEEE Transaction on Microwave Theory and Techniques. 2011:1769-1777. DOI: 10.1109/tmtt.2011.2140125

[11] Contreras A, Ribó M, Pradell L, Casals-Terré J, Giacomozzi F, Iannacci J. K-band RF-MEMS uniplanar reconfigurable-bandwidth bandpass filter using multimodal immittance inverters. Electronics Letters. 2013:704-706. DOI: 10.1049/el.2013.0681

[12] Mansour RR. RF MEMS-CMOS device integration: An overview of the potential for RF researchers. IEEE Microwave Magazine. 2013:39-56. DOI: 10.1109/MMM.2012.2226539

[13] Bakri-Kassem M, Fouladi S, Mansour RR. Novel high-Q MEMS curled-plate variable capacitors fabricated in 0.35-μm CMOS technology. IEEE Transaction on Microwave Theory and Techniques. 2008:530-541. DOI: 10.1109/TMTT.2007.914657

[14] Fouladi S, Mansour RR. Capacitive RF MEMS switches fabricated in standard 0.35-mm CMOS technology. IEEE Transaction on Microwave Theory and Techniques. 2010:478-486. DOI: 10.1109/TMTT.2009.2038446

[15] Riverola M, Uranga A, Torres F, Barniol N, Marigó E, Soundara-Pandian M. A reliable fast miniaturized RF MEMS-on-CMOS switched capacitor with zero-level vacuum package. In: 2017 IEEE MTT-S International Microwave Workshop Series on Advanced Materials and Processes for RF and THz Applications (IMWS-AMP); September 2017. pp. 1-3

[16] Kaynak M, Ehwald KE, Drews J, Scholz R, Korndörfer F, Knoll D, Tillack B, Barth R, Birkholz M, Schulz K, Sun YM, Wolansky D, Leidich S, Kurth S, Gurbuz Y. BEOL embedded RF-MEMS switch for mm-wave applications. In: IEEE MTT-S International Electron Devices Meeting; December 2009; Baltimore/New York: IEEE; p. 1-4

[17] Kaynak M, Wietstruck M, Zhang W, Drews J, Barth R, Knoll D, Korndörfer F, Scholz R, Schulz K, Wipf C, Tillack B, Kaletta K, Suchodoletz MV, Zoschke K, Wilke M, Ehrmann O, Ulusoy AC, Purtova T, Liu G, Schumacher H. Packaged BiCMOS embedded RF-MEMS switches with integrated inductive loads. In: IEEE MTT-S International Microwave Symposium; June 2012; Montreal. New York: IEEE; p. 1-3

[18] Rynkiewicz P, Franc, A-L, Coccetti, F, Tolunay-Wipf, S, Wietstruck M, Kaynak M, Prigent G. Tunable dual-mode ring filter based on BiCMOS embedded MEMS in V-band. In: Asia Pacific Microwave Conference; November 2017; Kuala Lumpur/New York: IEEE; p. 124-127

[19] Rebeiz GM. RF MEMS, Theory, Design and Technology. Hoboken: Wiley; 2003. 483p. DOI: 10.1002/0471225282

[20] Giacomozzi F, Mulloni V, Colpo S, Iannacci J, Margesin B, Faes A. A flexible fabrication process for the fabrication of RF MEMS devices. In: International Semiconductor Conference; Octuber 2011; Sinaia. pp. 155-158

[21] Benoit RR, Barker NS. Superconducting tunable microstrip gap resonators using low stress RF MEMS fabrication process. Journal of the Electron Devices Society. 2017:239-243. DOI: 10.1109/JEDS.2017.2706676

[22] Pelliccia L, Farinelli P. Sorrentino R. High- tunable waveguide filters using Ohmic RF MEMS switches. IEEE Transaction. on Microwave Theory and Techniques. 2015:3381-3390. DOI: 10.1109/TMTT.2015.2459689

[23] Shah U, Reck T, Frid H, Jung-Kubiak C, Chattopadhyay G, Mehdi I, Oberhammer J. A 500-750 GHz RF MEMS waveguide switch. IEEE Transactions on Terahertz Science and Technology. 2017:326-334. DOI: 10.1109/TTHZ.2017.2670259

[24] Tolunay-Wipf S, Göritz A, Wipf C, Wietstruck M, Burak A, Türkmen E, Gürbüz Y, Kaynak M. 240 GHz RF-MEMS Switch in a 0.13 μm SiGe BiCMOS Technology. In: IEEE Bipolar/BiCMOS Circuits and Technology Meeting; October 2017; Miami. pp. 54-57

[25] Nadaud K, Roubeau F, Pothier A, Blondy P, Zhang L-Y, Stefanini R. High Q zero level packaged RF-MEMS switched capacitor arrays. In: 11th European Microwave Integrated Circuits Conference; Octuber 2016; London/New York: IEEE; p. 448-451

[26] Young WC, Budynas RG, Sadegh AM. Roak's Formulas for Stress and Strain. 8th ed. New York: McGraw-Hill; 2012

[27] Wong WC, Azid IA, Majlis BY. Theoretical analysis of stiffness constant and effective mass for a round-folded beam in MEMS accelerometer. Journal of Mechanical Engineering. 2011;**57**:517-525. DOI: 10.5545/sv-jme.2009.151

[28] Fedder GK. Simulation of microelectromechanical systems [thesis]. Berkeley: Department of EECS University of California; 1994

[29] Contreras A, Casals-Terre J, Pradell L, Ribó M, Heredia J, Giacomozzi F, Margesin B. RF-MEMS switches for a full control of the propagating modes in uniplanar microwave circuits and their application to reconfigurable multimodal microwave filters. Microsystem Technologies. 2017:5959-5975. DOI: 10.1007/s00542-017-3379-8

[30] Llamas, MA, Girbau D, Pradell L, Lázaro A, Giacomozzi F, Colpo S. Characterization of Dynamics in RF-MEMS Switches. In: 10th International Symposium. RF MEMS and RF Microsystems (MEMSWAVE); 6-8 July 2009; Trento. pp. 117-120

[31] Fargas-Marques A, Casals-Terre J, Shkel A. Resonant pull-in condition in parallel-plate electrostatic actuator. Journal of Microelectromechanical Systems. 2007:1044-1053. DOI: 10.1109/JMEMS.2007.900893

[32] Casals-Terre J, Fargas-Marques A, Shkel A. Snap-action Bistable micromechanisms actuated by nonlinear resonance. Journal of Microelectromechanical Systems. 2008:1082-1093. DOI: 10.1109/JMEMS.2008.2003054

[33] Elata D, Bamberger H. On the Dynamic Response of Electrostatic MEMS Switches. Journal of Microelectromechanical Systems. 2008:236-243. DOI: 10.1109/JMEMS.2007.908752

[34] Leus V, Elata D. A new efficient method for simulating the dynamic response of electrostatic switches. In: 22nd International Conference on Micro Electro Mechanical Systems (MEMS); January 2009; Sorrento. New York: IEEE; p. 1115-1118

[35] Casals-Terre J, Llamas MA, Girbau Pradell L, Lázaro A, Giacomozzi F, Colpo S. Analytical energy model for the dynamic behavior of RF MEMS switches under increased actuation voltage. Journal of Microelectromechanical Systems. 2014:1428-1439. DOI: 10.1109/JMEMS.2014.23147

[36] Contreras A, Casals-Terré J, Pradell L, Giacomozzi F, Colpo S, Iannacci J, Ribó M. A RF-MEMS switchable CPW air-bridge. In: 7th European Microwave Integrated Circuits Conference; October 2012; Amsterdam/New York: IEEE; p. 441-444

[37] Ribó M, Pradell L. Circuit model for mode conversion in coplanar waveguide asymmetric shunt impedances. Electronics Letters. 1999:713-715. DOI: 10.1049/el:19990507

[38] Ribó M, de la Cruz J, Pradell L. Circuit model for slotline-to-coplanar waveguide asymmetrical transitions. Electronics Letters. 1999;1153-1155. DOI: 10.1049/el:19990779

[39] Ribó M, Pradell L. Circuit model for coplanar-slotline tees. IEEE Microwave Guided Wave Letters. 2000:177-179. DOI: 10.1109/75.850369

[40] Ribó M, Pradell L. Circuit model for a coplanar –Slotline cross. IEEE Microwave Guided Wave Letters. 2000:511-513. DOI: 10.1109/75.895085

[41] Gaddi R, Bellei M. Gnudi A, Margesin B, Giacomozzi F. Low-Loss Ohmic RF-MEMS Switches with Interdigitated Electrode Topology. In: Symposium on design, test, Integration and Packaging of MEMS/MOEMS (DTIP 2004); 2004. pp. 161-166

[42] Farinelli P, Margesin B, Giacomozzi F, Mannocchi G, Catoni S, Marcelli R, Mezzanotte P, Vietzorreck L, Vitulli F, Sorrentino R, Deborgies F. A low contact-resistance winged-bridge RF-MEMS series switch for wide-band applications. Journal of the European Microwave Association. 2007;**3**:268-278

[43] Calaza C, Margesin B, Giacomozzi F, Rangra K, Mulloni V. Electromechanical characterization of low actuation voltage RF MEMS capacitive switches based on DC CV measurements. Microelectronic Engineering. 2007:1358-1362. DOI: 10.1016/j.mee.2007.01.196

[44] Mulloni V, Solazzi F, Resta G, Giacomozzi F, Margesin B. RF-MEMS switch design optimization for long-term reliability. Analog Integrated Circuits and Signal Processing. 2014:323-332. DOI: 10.1007/s10470-013-0220-x

[45] De Angelis G, Lucibello A, Proietti E, Marcelli R, Bartolucci G, Casini F, Farinelli P, Mannocchi G, Di Nardo S, Pochesci D, Margesin B, Giacomozzi F, Vendier O, Kim T, Vietzorreck L. RF MEMS ohmic switches for matrix configurations. International Journal of Microwave and Wireless Technologies. 2012:421-433. DOI: 10.1017/S1759078712000074

[46] Diaferia F, Deborgies F, Di Nardo S, Espana B, Farinelli P, Lucibello A, Marcelli R, Margesin B, Giacomozzi F, Vietzorreck L, Vitulli F. Compact 12×12 switch matrix integrating RF MEMS switches in LTCC hermetic packages. In: 44th IEEE European Microwave Conference; 6-9 October 2014. Rome/New York: IEEE; p. 199-202

[47] Bastioli S, Di Maggio F, Farinelli P, Giacomozzi F, Margesin B, Ocera A, Pomona I, Russo M, Sorrentino R. Design and Manufacturing of a 5-bit MEMS Phase Shifter at K-band. In: European microwave In: Integrated Circuit Conference (EuMIC 2008); 27-30 October 2008. Amsterdam/New York: IEEE; p. 338-341

[48] Bedani M, Carozza F, Gaddi R, Gnudi A, Margesin B, Giacomozzi F. A reconfigurable impedance matching network employing RF-MEMS switches. In: Symposium on Design, Test, Integration and Packaging of MEMS and MOEMS (DTIP); 25-27 April 2007; Stressa

[49] Gaddi R, Gnudi A, Franchi E, Guermandi D, Tortori P, Margesin B, Giacomozzi F. Reconfigurable MEMS-enabled LC-tank for multi-band CMOS oscillator. In: IEEE MTT-S International Microwave Symposium; 17 June 2005; Long Beach. New York: IEEE. pp. 1353-1356

[50] Cazzorla A, Farinelli P, Urbani L, Cacciamani F, Pelliccia L, Sorrentino R, Giacomozzi F, Margesin B. MEMS-based LC tank with extended tuning range for low phase-noise VCO. International Journal of Microwave Wireless Technologies. 2017:249-258. DOI: 10.1017/S1759078715001579

[51] Giacomozzi F, Mulloni V, Colpo S, Faes A, Sordo G, Girardi S. RF-MEMS packaging by using quartz caps and epoxy polymers. Microsystem Technologies. 2014;**12**:1941-1948. DOI: 10.1007/s00542-014-2256-y

[52] Giacomozzi F, Iannacci J. RF MEMS technology for next-generation wireless communications. In: Handbook of Mems for Wireless and Mobile Applications. Woodhead Publishing; 2013. pp. 225-257. DOI: 10.1533/9780857098610.1.225

[53] Alameh AA, Nabki F. A 0.13-μm CMOS dynamically reconfigurable charge pump for electrostatic MEMS actuation. IEEE Transaction on Very Large Scale Integration Systems (VLSI). 2017:1261-1270. DOI: 10.1109/ICECS.2014.7050074

[54] Ismail Y, Lee H, Pamarti S, Yang C-KK. A 34V charge pump in 65nm bulk CMOS technology. In: IEEE International Solid-State Circuits Conference; February 2014; San Francisco. New York: IEEE. pp. 408-409

[55] Sattler R, Plötz F, Fattinger G, Wachutka G. Modeling of an electrostatic torsional actuator: Demonstrated with an RF MEMS switch. Sensors Actuators A: Physical. 2002:337-346. DOI: 10.1016/S0924-4247(01)00852-4

[56] Mercier D, Blondy P, Pothier A. Monitoring mechanical characteristics of MEMS switches with a microwave test bench. In: ESA-ESTEC 4th Round Table on Micro/Nano Technologies for Space; May 2003

[57] Llamas MA, Ribó M, Girbau D, Pradell L. A rigorous multimodal analysis and design procedure of a uniplanar 180° hybrid. IEEE Transaction on Microwave Theory Techniques. June 2009;**16**:1832-1839. DOI: 10.1109/TMTT.2009.2022881

[58] Contreras A, Ribó M, Pradell L, Blondy P. Uniplanar bandpass filters based on multimodal immitance inverters and end-coupled slotline resonators. IEEE Transaction on Microwave Theory Techniques. 2013:77-88. DOI: 10.1109/TMTT.2012.2226743